J. Fluid Mech. (2010), *vol.* 646, *pp.* 207–231. © Cambridge University Press 2010
doi:10.1017/S0022112009992837

Coherent structures in wave boundary layers. Part 2. Solitary motion

B. MUTLU SUMER[1]†, PALLE M. JENSEN[1], LONE B. SØRENSEN[1], JØRGEN FREDSØE[1], PHILIP L.-F. LIU[2] AND STEFAN CARSTENSEN[1]‡

[1]Technical University of Denmark, DTU Mekanik, Section of Coastal, Maritime and Structural Engineering, Building 403, 2800 Kgs. Lyngby, Denmark

[2]School of Civil and Environmental Engineering, Cornell University, Ithaca, NY 14853, USA

(Received 19 September 2008; revised 16 October 2009; accepted 18 October 2009)

This study continues the investigation of wave boundary layers reported by Carstensen, Sumer & Fredsøe (*J. Fluid Mech.*, 2010, part 1 of this paper). The present paper summarizes the results of an experimental investigation of turbulent solitary wave boundary layers, simulated by solitary motion in an oscillating water tunnel. Two kinds of measurements were made: bed shear stress measurements and velocity measurements. The experiments show that the solitary-motion boundary layer experiences three kinds of flow regimes as the Reynolds number is increased: (i) laminar regime; (ii) laminar regime where the boundary-layer flow experiences a regular array of vortex tubes near the bed over a short period of time during the deceleration stage; and (iii) transitional regime characterized with turbulent spots, revealed by single/multiple, or, sometimes, quite dense spikes in the bed shear stress traces. Supplementary synchronized flow visualization tests confirmed the presence of the previously mentioned flow features. Information related to flow resistance are also given in the paper.

1. Introduction

Although much research has been carried out on boundary layers under harmonic progressive waves (see Carstensen, Sumer & Fredsøe 2010, part 1 of this paper, for an extensive review), to the authors' knowledge, Liu, Park & Cowen (2007) were the first to study boundary-layer flows under solitary waves in details. They derived analytical solutions, based on (i) those of Liu & Orfilla (2004) for viscous boundary-layer flows under transient long waves, and (ii) the solutions for the nonlinear boundary-layer equations. They also carried out laboratory measurements that include the free-surface displacement, particle image velocimetry (PIV)-resolved velocity fields of the boundary layer and the bottom shear stress. Liu *et al.* (2007) gave a detailed account of the existing work on the subject prior to their study, notably Keulegan (1948) and Mei (1983). Tanaka, Sumer & Lodahl (1998), in their work on laminar boundary layers under cnoidal waves, derived equations for the time variations of the velocity and the bottom shear stress for solitary waves (which they viewed as the asymptotic

† Email address for correspondence: bms@mek.dtu.dk
‡ Present address: DHI, Agern Alle 5, 2970 Hørsholm, Denmark.

https://doi.org/10.1017/S0022112009992837 Published online by Cambridge University Press

case of cnoidal waves as the Ursell parameter goes to infinity), using Keulegan's (1948) analytical solution.

Regarding turbulent solitary-wave boundary-layer flows, in an earlier study, Liu (2006) developed analytical solutions to the wave damping due to a turbulent boundary layer. In a recent study, Vittori & Blondeaux (2008*a* and 2008*b*) presented the results of an investigation in which turbulent boundary layer under a solitary wave was studied by direct numerical simulations (DNSs). The latter study is discussed in detail in this paper.

In part 1 of this paper, wave boundary layer over a smooth bed was studied under oscillatory motion. The focus was on the transitional regimes of the oscillatory boundary-layer flows. This study extends the work described in part 1 to solitary wave boundary layers. To this end, the solitary wave boundary-layer flow is simulated in the laboratory in an oscillating water tunnel. With this, the wave-induced velocities can be increased quite substantially, up to 1.2 $\mathrm{m\,s^{-1}}$ in the present facility, resulting in Re numbers up to 2×10^6, the Reynolds numbers that cannot be achieved in ordinary, small- or medium-scale wave-flume facilities. (Here Re is defined, based on (i) the maximum value of the free-stream velocity outside the boundary layer, and (ii) the half of the stroke of the water particle displacement in the free-stream region under the solitary wave; (7).) It turns out that the boundary-layer flow experiences tremendous changes (laminar, laminar with vortex tubes near the bed, laminar-to-turbulence transition, and turbulence), as Re is increased from laminar- to turbulent-regime Reynolds numbers. (Some early results of this study have been presented at the 18th ISOPE Conference; Sumer *et al.* 2008.)

2. Experimental facility

2.1. *The oscillating water tunnel and instrumentation*

The experiments were carried out in the same U-shaped oscillating water tunnel as in part 1 (figure 1 in part 1). The solitary motion in the tunnel was driven by the same electronically controlled pneumatic system. The piston of the pneumatic system in the present experiments was driven such that the free-stream velocity in the tunnel satisfied

$$U_0 = U_{0m}\mathrm{sech}^2(\omega t), \tag{1}$$

the variation of the particle velocity at the bed at a given location under a small-amplitude solitary wave. Here ω is the angular frequency

$$\omega = \frac{2\pi}{T}, \tag{2}$$

(where the quantity T can be interpreted as the period of the motion, a time scale that characterizes the width of the velocity time series; figure 1*a*). In the tests, the piston was moved in the direction of the open riser (figure 1 in part 1), and stopped at the instant when the water reached the top of the open riser. Figure 2 displays a time series of the measured free-stream velocity (time series 2). The portion of the data with negative velocities at the trailing end of $U_0(t)$ (i.e. time series 2 beyond the cutoff phase in figure 2) was disregarded in the data analysis, t_{cutoff} corresponding to $\omega t_{cutoff} \simeq 100^\circ$, or slightly larger (cf. figure 1).

The measurements were made at the same section as that in part 1 (figure 1 of part 1). Two kinds of measurements were performed: bed shear stress measurements

https://doi.org/10.1017/S0022112009992837 Published online by Cambridge University Press

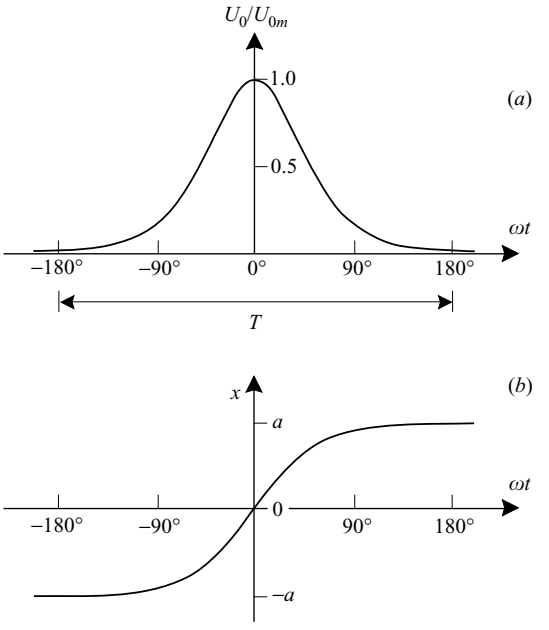


FIGURE 1. (*a*) Variation of the free-stream velocity and (*b*) the water particle displacement in the free-stream region in a solitary motion.

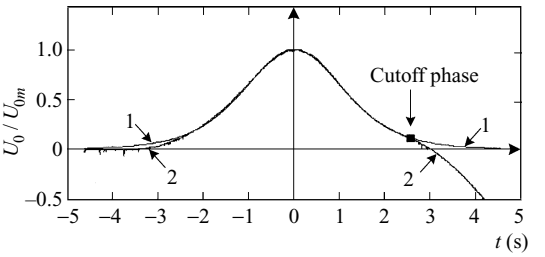


FIGURE 2. Free-stream velocity. (1) Equation (1) and (2) measured time series in the experiment.

and velocity measurements. The bed shear stress was measured, using the same hot-film probe as in part 1. The streamwise velocity was measured with a laser doppler anemometer (LDA), used in the forward scatter mode. The LDA was a Dantec model 60×11 fibre optic head equipped with a 430 mW argon laser, a Dantec 55N12 frequency shifter and a Dantec 55N20 frequency tracker. The dimensions of the measuring volume were $(d_x \times d_y \times d_z) = 0.66\,\text{mm} \times 0.078\,\text{mm} \times 0.078\,\text{mm}$.

Two velocity measurements were made with the LDA: (i) Velocity measurements at $y = 0.4$ mm just above the hot-film probe, to 'monitor' the direction of the bed shear stress, as the hot-film probe does not sense the direction. The experiments showed that the velocity at the measurement point ($y = 0.4$ mm from the bed) lagged behind the bed shear stress about 10° under laminar conditions (in agreement with the laminar theory; Liu *et al.* 2007), while practically no phase difference was observed between the two signals (the velocity and the bed shear stress signals) under turbulent conditions. (ii) Velocity measurements at several y locations from the bed (at the centre of the flume width) with the purpose of determining the mean and turbulence

https://doi.org/10.1017/S0022112009992837 Published online by Cambridge University Press

characteristics of the motion as a function of the distance from the bed (tests 3, 9 and 14 in table 1).

A program was written in MatLab, using the Data Acquisition Toolbox, which included functions such as controlling/driving the pneumatic system and sampling bed shear stress and velocity data. This was different from the way in which the pneumatic system was controlled and the data were sampled in part 1. In the present system, as the controlling of the pneumatic system and the sampling of data were achieved through the same software, there was no need to sample a reference signal. Rather the piston motion, generated by the software, acted as the reference signal in the data processing.

Mean values of the quantities (the bed shear stress or the velocity) are calculated through ensemble averaging according to

$$\overline{\phi}(\omega t) = \frac{1}{N}\sum_{j=1}^{N}[\phi(\omega t)]_j \tag{3}$$

in which $[\phi(\omega t)]_j$ is the time series of ϕ obtained in run j, and N is the total number of runs (i.e. the sample size). The root-mean-square (r.m.s.) value of the fluctuating component of the quantity in question, $\phi' = \phi - \overline{\phi}$, is calculated by

$$(\overline{\phi'^2})^{1/2}(\omega t) = \left\{\frac{1}{N-1}\sum_{j=1}^{N}\left\{[\phi(\omega t)]_j - \overline{\phi}(\omega t)\right\}^2\right\}^{1/2} \tag{4}$$

2.2. *Flow visualization*

Although the main focus of this study was the statistical properties of the hydrodynamic quantities such as the bed shear stress and the streamwise velocity, some limited number of flow visualization experiments were made to complement the bed shear stress and velocity measurements. Similar to part 1, two types of flow visualizations were carried out: (i) plan-view flow visualization, and (ii) side-view flow visualization. The methods used in these experiments were exactly the same as in part 1. The flow visualizations were made synchronized with the bed shear stress measurements. Details regarding the flow visualization technique, the synchronization and the equipment are described in part 1.

3. Test conditions

Table 1 summarizes the test conditions. The quantities T and U_{0m} in table 1 are the period and the maximum value of the free-stream velocity, respectively ((1) and (2)). The procedure to obtain these quantities was as follows. (i) Switch on the solitary motion from rest; (ii) Sample the free-stream velocity $U_0(t)$; (iii) Fit (1) to the measured velocity time series $U_0(t)$; and (iv) From this, obtain U_{0m} and ω; and from (2), get T.

The quantity a in table 1 is half of the stroke of the water particle displacement in the free-stream region

$$x = a\tanh(\omega t) \tag{5}$$

(figure 1*b*), and found from

$$a = \frac{U_{0m}}{\omega} \tag{6}$$

https://doi.org/10.1017/S0022112009992837 Published online by Cambridge University Press

https://doi.org/10.1017/S0022112009992837 Published online by Cambridge University Press

Test no.	Period, T (s)	Maximum value of velocity, U_{0m} ($\mathrm{m\,s^{-1}}$)	Half-stroke, a (m)	$Re = aU_{0m}/\nu$	Stokes length $\delta_1 = (2\nu/\omega)^{1/2}$ (cm)	Quantity measured	Sample size (number of realizations), N
1	7.0	0.14	0.20	2.8×10^4	0.15	τ_0, U_0	5
2	8.4	0.21	0.28	5.9×10^4	0.16	τ_0, U_0	5
3	8.2	0.22	0.28	7.1×10^4	0.16	$u(y)$ (accompanied by τ_0 measured)	5 at each measured point
4	8.8	0.25	0.38	9.4×10^4	0.17	τ_0, U_0	2
5	9.2	0.36	0.55	2.0×10^5	0.17	τ_0, U_0	30
6	9.3	0.41	0.65	2.7×10^5	0.17	τ_0, U_0	21
7	8.9	0.45	0.68	3.1×10^5	0.17	τ_0, U_0	31
8	9.4	0.53	0.83	4.4×10^5	0.17	τ_0, U_0	30
9	9.0	0.56	0.77	4.8×10^5	0.17	$u(y)$ (accompanied by τ_0 measured)	15 at each measured point
10	9.3	0.64	1.02	6.5×10^5	0.17	τ_0, U_0	30
11	8.8	0.82	1.29	1.1×10^6	0.17	τ_0, U_0	30
12	8.3	0.96	1.38	1.3×10^6	0.16	τ_0, U_0	30
13	8.7	1.03	1.54	1.6×10^6	0.17	τ_0, U_0	30
14	7.8	1.20	1.50	1.8×10^6	0.16	$u(y)$ (accompanied by τ_0 measured)	15 at each measured point
15	7.9	1.19	1.64	2.0×10^6	0.16	τ_0, U_0	30

TABLE 1. Test conditions. Water temperature was 20°C. Kinematic viscosity was $1.0 \times 10^{-2}\,\mathrm{cm^2\,s^{-1}}$.

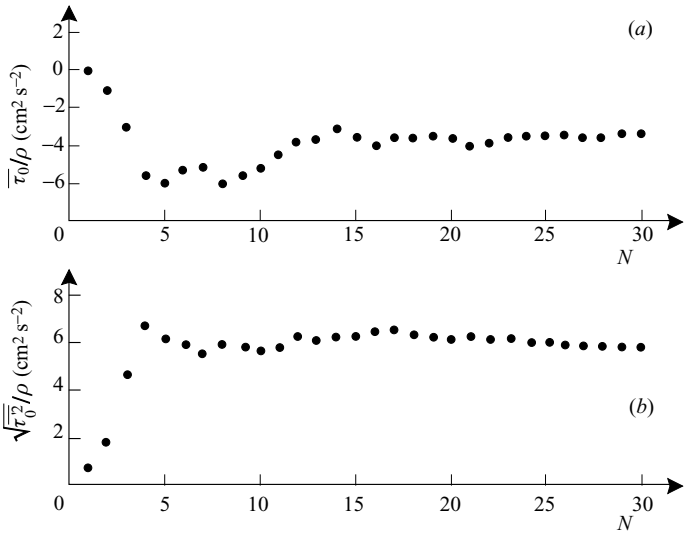


FIGURE 3. Sensitivity to the number of waves. (*a*) Mean and (*b*) standard deviation of the bed shear stress. $\omega t = 64.4^\circ$ (where the turbulence is largest). $Re = 1.1 \times 10^6$.

Re in table 1 is the Reynolds number defined by

$$Re = \frac{aU_{0m}}{\nu} \tag{7}$$

similar to the oscillatory flow case. As seen from the table, the maximum Re number tested in the experiments is 2×10^6. Reynolds numbers larger than this value could not be achieved due to the limited stroke length of the piston of the pneumatic system (figure 1, part 1). The quantity δ_1 in table 1 is the Stokes length defined by

$$\delta_1 = \sqrt{\frac{2\nu}{\omega}}, \tag{8}$$

similar to the case of oscillatory boundary layers.

The sampling interval in the measurements was 4.17 ms. This corresponds to approximately 1900–2250 samples over the period of the motion (tests 1–15, table 1), and is large enough to be able to trace time development of the measured statistical quantities.

The number of runs, N, conducted for the bed shear stress measurements was 5 for tests 1 and 2, and 2 for test 4 in the laminar-regime experiments (table 1, last column). N was larger in tests 1 and 2 than that in test 4, to check the reproducibility of the results. Regarding the non-laminar-regime tests, a sensitivity analysis was carried out to determine the number of runs to get reliable ensemble averages. This analysis showed that the statistics (the mean value and the standard deviation) of the bed shear stress converged when $N \gtrapprox 15$ for $Re = 4.4 \times 10^5$, $N \gtrapprox 15$ for $Re = 1.1 \times 10^6$ and $N \gtrapprox 25$ when $Re = 2 \times 10^6$. Therefore N was, for the most part, chosen as 30 for the non-laminar-regime experiments (tests 5–8, 10–13 and 15, last column in table 1). Figure 3 depicts an example of the sensitivity analysis where the mean and the standard deviation of the bed shear stress are plotted as a function of the sample size for $\omega t = 64.4^\circ$, the phase where the turbulence is largest.

Regarding the velocity-profile measurements, these measurements were carried out at 20 points across the depth covering the half-height of the tunnel. In order to

https://doi.org/10.1017/S0022112009992837 Published online by Cambridge University Press

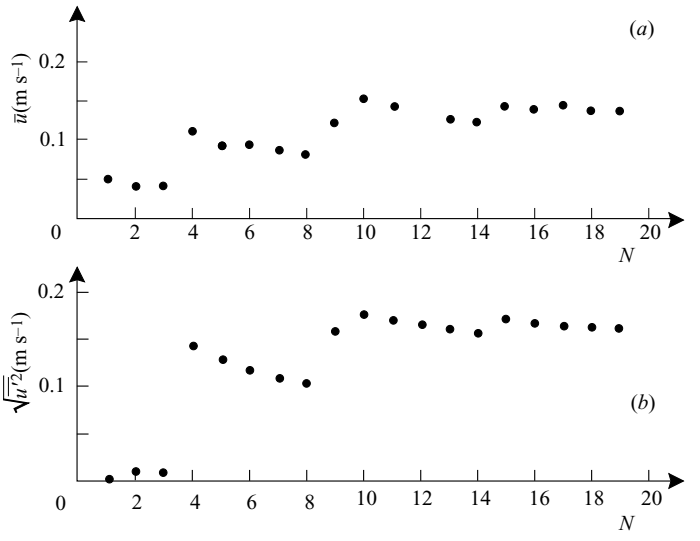


FIGURE 4. Sensitivity to the number of waves. (*a*) Mean and (*b*) standard deviation of the streamwise velocity. $\omega t = 30^\circ$ (where the turbulence is largest). $Re = 1.8 \times 10^6$ and $y = 0.6$ mm ($y^+ = 22.7$).

check the convergence of the statistics, a sensitivity analysis was carried out for $Re = 1.8 \times 10^6$ (the highest Re for the velocity measurements) at the phase value $\omega t = 30^\circ$, the phase value where the turbulence is largest. This analysis showed that the statistics converged when $N \gtrapprox 15$. Therefore, $N = 15$ runs were conducted for each Reynolds number in the non-laminar-regime experiments (tests 9 and 14, table 1). For the laminar-regime experiments N was chosen as 5 (test 3, table 1). With regard to the turbulent-regime experiments, the number of runs was kept at the minimum required for the convergence, $N = 15$, a relatively low value compared with the bed shear stress measurements. This was essentially a 'trade-off', considering the very high number of velocity measurements (15 measurements at each measurement point involving 20 measurement points across the depth). Figure 4 gives an example of the sensitivity analysis carried out for the velocity for $\omega t = 30^\circ$, the phase where the turbulence is largest, similar to figure 3. The data in figure 4 are for the measurement point $y = 0.6$ mm ($y^+ = 22.7$).

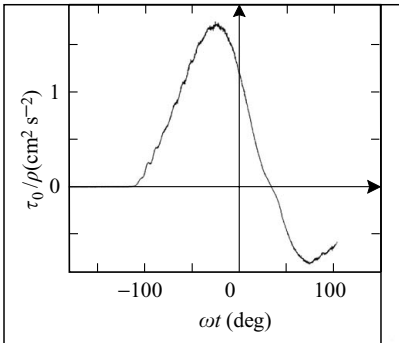
4. Bed shear stress

4.1. *Flow regimes*

The boundary-layer flow developing over a smooth bed of a solitary motion in the half-space $y > 0$ is described by a single parameter, the Reynolds number, (7), similar to oscillatory boundary layers. The boundary-layer flow undergoes tremendous changes as the Reynolds number is increased. The flow regimes experienced with increasing Reynolds number is summarized in figure 5 with reference to sampled bed shear stress traces. In the figures, τ_0 is the bed shear stress and ρ the water density.

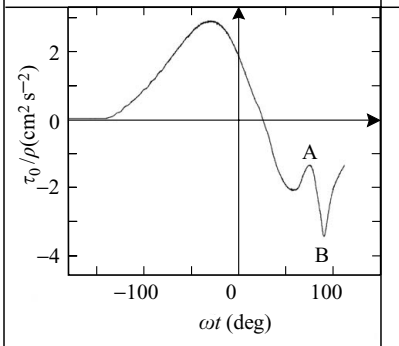
(We note that, in the case of a solitary-motion boundary layer developing in a finite-depth flow environment rather than the half-space $y > 0$, the boundary layer is described by two parameters, namely the Reynolds number and the boundary-layer-thickness-to-depth ratio. Vittori & Blondeaux (2008*b*) chose the following set

https://doi.org/10.1017/S0022112009992837 Published online by Cambridge University Press



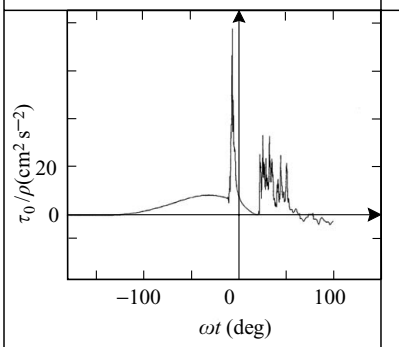
	Laminar	$Re < 2\times10^5$

(*a*)



	Laminar with vortex tubes	$2\times10^5 \leq Re < 5\times10^5$

(*b*)



	Transitional	$5\times10^5 < Re <$???

(*c*)

No bed shear stress trace is available as this regime could not be achieved in the present experiments due to experimental constraints. However, it is expected that turbulence spreads over the entire phase space, similar to the bed shear stress trace presented in figure 16*d* in part 1of this paper for the case of oscillatory motion.	Fully developed turbulent	??? < *Re*

(*d*)

FIGURE 5. Flow regimes with reference to sample time series of the bed shear stress. Sample time series for (*a*) $Re = 9.4\times10^4$, (*b*) $Re = 3.1\times10^5$, (*c*) $Re = 2.0\times10^6$.

of parameters for real solitary wave boundary layers, H/h and δ_{VB}/h, in which h is the water depth, H the wave height, δ_{VB} the boundary-layer thickness defined by $\delta_{VB} = \sqrt{(2\nu h)/(\sqrt{gh})}$. Vittori & Blondeaux's set of parameters can be converted to the previously mentioned set of parameters, as has been done in the present study in conjunction with the transition to turbulence; § 4.4.)

https://doi.org/10.1017/S0022112009992837 Published online by Cambridge University Press

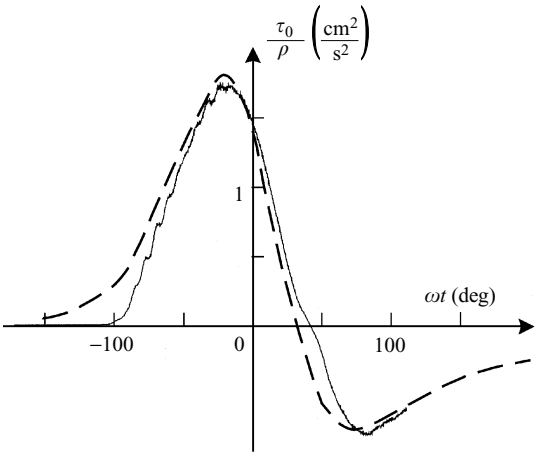


FIGURE 6. Comparison between the experimentally obtained time series of the bed shear stress and the laminar solution of Liu *et al.* (2007). Test 4 (table 1, $Re = 9.4 \times 10^4$).

For Re numbers up to 2×10^5, the flow is laminar (figure 5*a*); no sign of turbulence is observed in the bed shear stress signal. When Re is increased further, typically a strong decrease in magnitude (A, figure 5*b*), followed by a strong increase (B), emerges in the bed shear stress signal; this flow regime falls into the Reynolds number range $2 \times 10^5 \leqslant Re < 5 \times 10^5$. As demonstrated below, this behaviour is related to the emergence of quasi-two-dimensional vortex tubes, the coherent flow feature studied in detail in part 1. With a further increase in the Reynolds number, for Re larger than 5×10^5 up to $Re = 2 \times 10^6$ (the highest Reynolds number achieved in the present experiments), the bed shear stress experiences single or multiple or sometimes quite dense spikes, produced by the passage of turbulent spots over the measuring point (figure 5*c*), first emerging towards the end of the flow period, and gradually spreading to earlier phase of the motion with increasing Re, in the same way as in the oscillatory motion (c.f. part 1). This regime corresponds to the transitional flow regime.

For even further increase in the Reynolds number ($Re > 2 \times 10^6$), the previously described spikes are expected to spread over practically the entire phase space, and with this, the flow is expected to become fully developed turbulent, similar (qualitatively) to the case of oscillatory boundary layers (Jensen, Sumer & Fredsøe 1989; Lodahl, Sumer & Fredsøe 1998; and part 1 of this study). Further discussion on this aspect of the problem is given in § 4.4.

4.2. *Laminar regime* ($Re < 2 \times 10^5$)

Figure 6 shows the time series of the measured bed shear stress in test 4 (table 1, $Re = 9.4 \times 10^4$), plotted together with the laminar solution of Liu *et al.* (2007). The figure shows that the agreement is good although the measured bed shear stress deviates from the analytical solution for the phase values $\omega t < O(-100^\circ)$. This is not entirely unexpected, considering the discrepancy between the experimentally generated velocity and the theoretical expression of the solitary motion observed in figure 2 during the initial stage of the motion. (We note that Liu *et al.* (2007) in their laminar boundary-layer experiments in a wave flume also obtained a good agreement between their prediction and their bed-shear stress measurements.)

As seen, the bed shear stress leads over the free-stream velocity (in agreement with the oscillatory boundary-layer flows; see e.g. Fredsøe & Deigaard 1992), and

https://doi.org/10.1017/S0022112009992837 Published online by Cambridge University Press

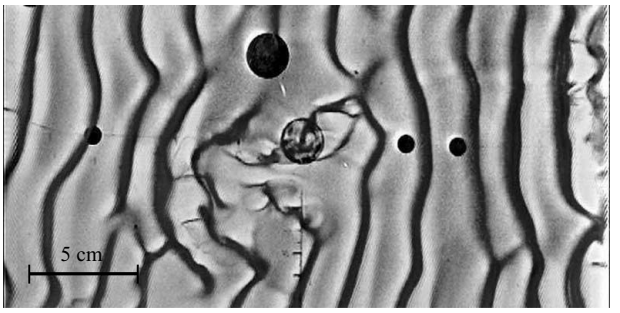


FIGURE 7. A video frame illustrating the vortex tubes in plan view at $\omega t = 93°$. $U_{0m} = 50.9\,\mathrm{cm\,s^{-1}}$, $T = 9.3$ s, $Re = 3.8 \times 10^5$.

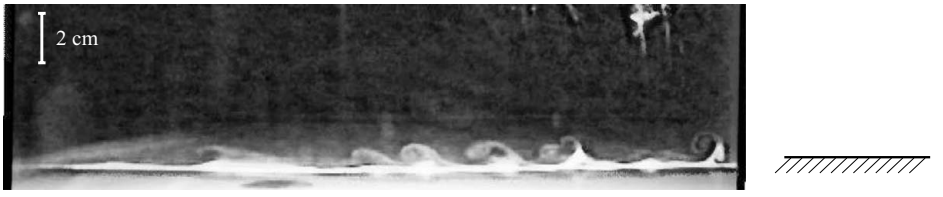


FIGURE 8. A video frame illustrating the vortex tubes in side view at $\omega t = 105.7°$. $U_{0m} = 43.9\,\mathrm{cm\,s^{-1}}$, $T = 9.2$ s, $Re = 2.8 \times 10^5$.

eventually it reverses at the phase $\omega t = 33°$, which agrees quite well with the analytical solution. The flow reversal is related to the driving pressure gradient $\partial p/\partial x$; this pressure gradient becomes positive (i.e. the flow experiences an adverse pressure gradient) in the deceleration period ($\omega t > 0°$). However, it takes $\omega t = 33°$ in phase for the flow adjacent to the bed to 'dissipate' its momentum and also to overcome the viscous resistance, to respond to the adverse pressure gradient. At this juncture, we note that Liu *et al.* (2007, figure 11) were the first to measure the bed shear stress in a solitary wave boundary layer. They made their measurements in a wave flume under real, solitary waves, with Re falling into the range of laminar-flow Reynolds numbers. (They used the PIV technique and obtained the bed shear stress by fitting a straight line to the velocity variation very close to the bed.) Liu *et al.*'s results show a very good agreement between the experimental data and their analytical prediction.

4.3. *Laminar regime with vortex tubes* ($2 \times 10^5 \leqslant Re < 5 \times 10^5$)

In the Reynolds number interval $2 \times 10^5 \leqslant Re < 5 \times 10^5$, typically a strong decrease (A, figure 5*b*), followed by a strong increase (B), emerges in the bed shear stress signal (figure 5*b*), as discussed above. This behaviour, which is clearly different from the pure laminar-regime flow, is related to the emergence of the vortex tubes, the coherent structures generated as a result of the inflectional-point shear layer instability studied in part 1 in conjunction with the oscillatory-motion boundary-layer flows. Figure 7 shows a video frame illustrating the vortex tubes in plan view ($Re = 3.8 \times 10^5$). Figure 8, on the other hand, shows another video frame for a side view of the vortex tubes obtained in another test ($Re = 2.8 \times 10^5$). See supplementary movies 1 and 2 at journals.cambridge.org/flm.

Now, the decrease (A) in the bed shear stress signal (figure 5*b*) corresponds to the situation where the bed shear-stress probe (the hot film) experiences the flow between two successive vortices (marked A in figure 9), while the increase (B) in figure 5*b* corresponds to the situation where the wall shear-stress probe experiences the next

https://doi.org/10.1017/S0022112009992837 Published online by Cambridge University Press

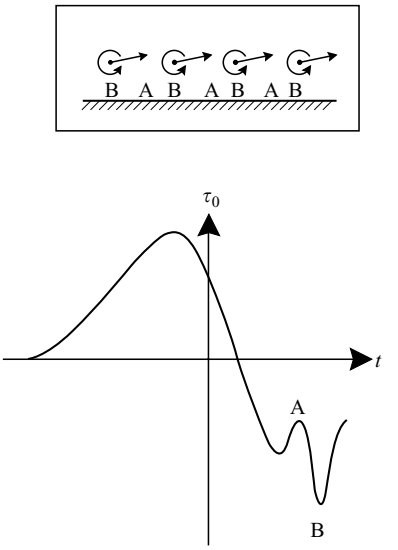


FIGURE 9. The time history of the bed shear stress in the laminar regime with vortex tubes.

vortex (marked B in figure 9) as the system of the vortex tubes is convected in the direction of the near-bed flow. This is precisely the same mechanism as discussed in part 1. As mentioned in part 1, these vortices are caused by the inflection-point instability mechanism. To the authors' knowledge, so far no study is available that investigates this instability (from the point of view of hydrodynamic instability theory) in the case of the boundary layer under solitary wave motion.

Four tests of the present experiments, tests 5–8, fall into the range $2 \times 10^5 \leqslant Re < 5 \times 10^5$ where the flow regime was laminar with vortex tubes. Of these tests, test 8 was presumably too close to the demarcation line between this regime and the laminar-to-turbulent transition regime, and therefore not in all runs, the bed shear stress behaved the same way as described in the preceding paragraphs, and there was sign of turbulence in the time histories of the bed shear stress in several cases. In the case of tests 5–7 (with $Re = 2 \times 10^5$, 2.7×10^5 and 3.1×10^5), however, all the time histories showed the same behaviour as described above. When plotted on top of each other (not shown here for reasons of space), the bed shear stress traces collapsed practically on a single curve meaning that, for a given Reynolds number, (i) the vortex tubes come into existence at exactly the same phase value, (ii) they travel with exactly the same speed, and (iii) they have exactly the same lifespan regardless of the test.

From the data, the mean phase values for the decrease (A, figure 5*b*) and that for the increase (B, figure 5*b*) are as follows:

Re	ωt (A in figure 5*b*)	ωt (B in figure 5*b*)
2.0×10^5	76°	94.5°
2.7×10^5	77°	100°
3.1×10^5	74°	90.5°

As seen, there is a slight increase in the phase values for $Re = 2.7 \times 10^5$. No clear explanation has been found for this behaviour.

https://doi.org/10.1017/S0022112009992837 Published online by Cambridge University Press

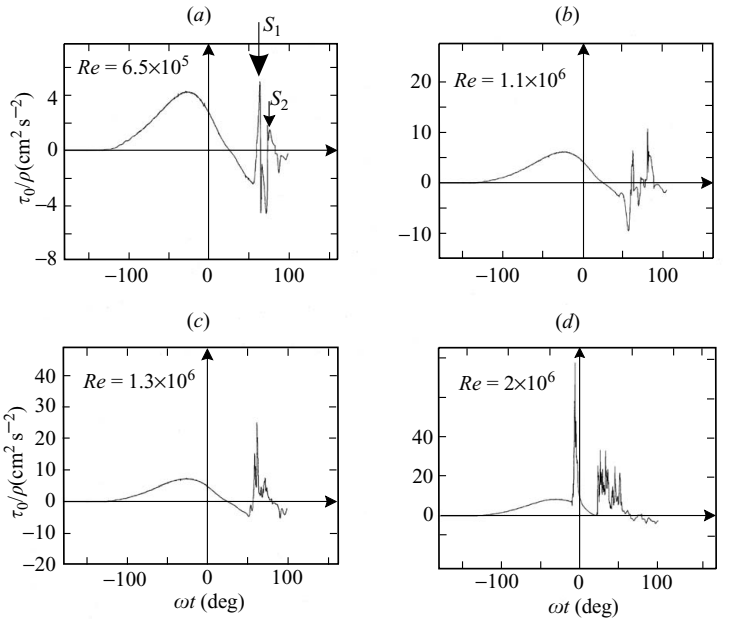


FIGURE 10. Four sample time histories of bed shear stress in the laminar-to-turbulent transition regime.

4.4. *Laminar-to-turbulent transition and the transitional regime* ($5 \times 10^5 < Re < ?$)

With a further increase in the Reynolds number, for Re larger than 5×10^5 up to 2×10^6 (the highest Reynolds number achieved in the present experiments), the bed shear stress experiences single or multiple or, sometimes, quite dense spikes, produced by the passage of turbulent spots over the measuring point (figure 5*c*), first emerging towards the end of the flow period, and gradually spreading to earlier phase of the motion with increasing Re, in the same way as in the case of the oscillatory-motion boundary-layer flows (part 1).

Figure 10 displays four sample traces for the measured bed shear stress, each corresponding to a different Reynolds number. Figure 10 shows that the bed shear stress experiences spikes, sometimes very dense, similar to the case of the oscillatory-motion boundary-layer flow studied in part 1. These spikes are caused by turbulent spots, as detailed in part 1. For example, in figure 10(*a*), the flow at the bed reverses at around $\omega t = 25°$. However, it then experiences a very strong spike (marked S_1) starting at $\omega t = 55°$, indicating that a turbulent spot (forming upstream of the hot film and travelling in the positive direction) hits the hot film, presumably changing the flow direction again at the bed. This is followed by a second, smaller spike (marked S_2), indicating that a second turbulent spot is passing overhead. It may be noted that there is a striking resemblance between the present bed shear stress history in figure 10(*a*) and that given in figure 2 of Vittori & Blondeaux (2008*b*) of the longitudinal velocity component, u_1, near the bed in the turbulent flow regime, with u_1 experiencing positive and negative spikes in the same manner as in figure 10(*a*). Figure 11 shows a video frame illustrating turbulent spots in plan view. See supplementary movie 3.

https://doi.org/10.1017/S0022112009992837 Published online by Cambridge University Press

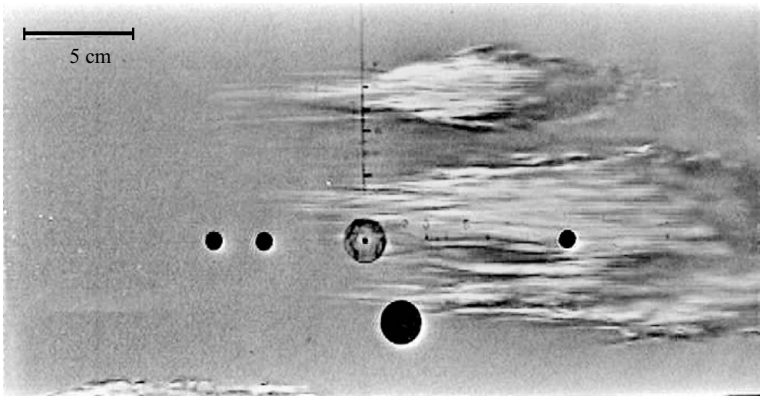


FIGURE 11. Video frame illustrating turbulent spots in plan view at $\omega t = 26.5°$. $U_{0m} = 93.9\,\mathrm{cm\,s^{-1}}$, $T = 7.8$ s, $Re = 1.1 \times 10^6$.

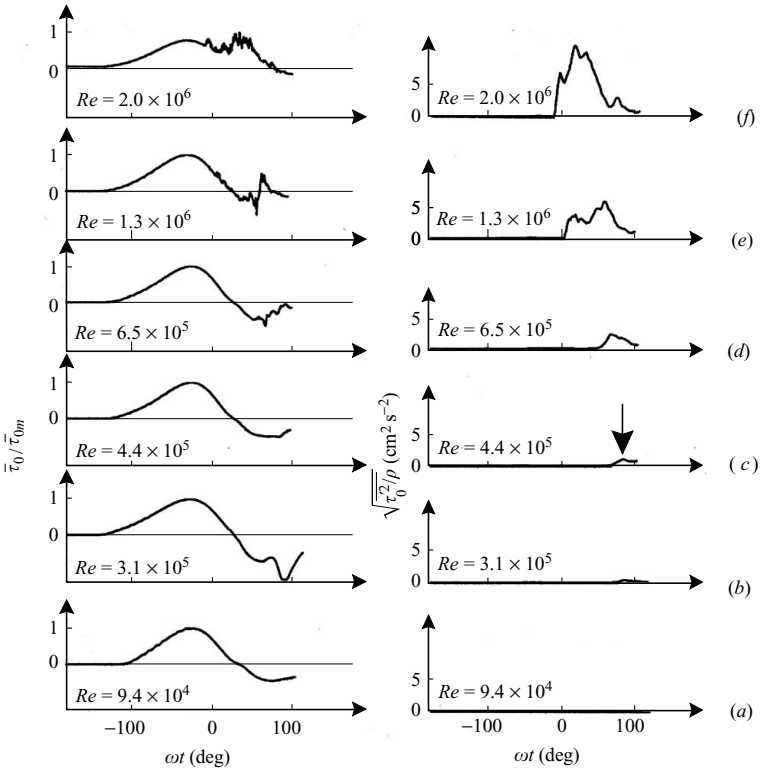


FIGURE 12. Time variation of the mean bed shear stress and that of the r.m.s. value of the fluctuations in the bed shear stress with increasing Reynolds number.

Similar to the oscillatory-motion boundary layers (part 1), the present plan-view flow visualization showed that turbulent spots and vortex tubes may occur concurrently. Video frames illustrating this will not be given here for reasons of space.

Figure 12 displays the phase variation of the mean bed shear stress (figure 12, left) and that of the r.m.s. value of the fluctuations in the bed shear stress (figure 12, right) for various Reynolds numbers. The r.m.s. values are not normalized to illustrate the

https://doi.org/10.1017/S0022112009992837 Published online by Cambridge University Press

growth of the turbulence as the Reynolds number is increased. It is remarkable how the mean and the r.m.s. profiles change shape as one proceeds through the Re range. (In connection with the statistics presented in figure 12, we note that the position of the turbulent spots relative to the measurement point is random (see part 1, figure 17 and the related text), and therefore the above statistics also implies a spatial spanwise mean on the spots.)

An interesting observation is that although several of the time histories obtained for $Re = 4.4 \times 10^5$ exhibited the same kind of variation as in figure 5(b), when ensemble averaged, the local crests and troughs observed in these time history records are smoothed out, and therefore the variation in figure 12(c) looks like the laminar profile as in figure 12(a). However, the variation from one time history to another for this Reynolds number manifests itself in the form of turbulence in the r.m.s. profile in figure 12(c) (marked with a vertical arrow). Another observation is that, for the higher Reynolds-number regimes (figure 12d–f) the spikes observed in the individual time histories of the bed shear stress (figure 10) also are smoothed out when the individual records are ensemble averaged. Note also that the maximum value of the mean bed shear stress in the turbulent regime with $Re = 2 \times 10^6$ (figure 12f, left) is not the one associated with the maximum value of the free-stream velocity, but rather the value associated with turbulent spots.

It is seen from figure 12 (right) that the occurrence of turbulence in the bed shear stress spreads towards the lower values of phase ωt, as Re is increased (figure 12, right, as we proceed from d to f). This is in good agreement with the results of Vittori & Blondeaux's (2008b, figure 3) numerical simulations where the latter authors plotted the turbulence energy, K, as a function of phase for various values of their non-dimensional parameter $\epsilon (= H/h)$, where H is the wave height and h the water depth. Their results show that K spreads towards earlier phase values as ϵ (or alternatively Re) increases.

As noted earlier, although not captured in the present study, turbulence is expected to spread towards even lower values of ωt as Re is increased further, eventually covering the entire phase range. Unfortunately, this higher Reynolds number regime could not be captured in the present study due to the finite stroke length of the piston of the pneumatic system (as pointed out earlier) to test this argument. One may note, however, that, in the case of the oscillatory boundary layers, the role of the turbulence left from the previous half-cycle is such that it will promote transition (trigger turbulence) in the boundary layer, as demonstrated experimentally by Fredsøe *et al.* (2003) and by DNSs of Costamagna, Vittori & Blondeaux (2003). Clearly, this 'background' turbulence does not exist in the case of the solitary motion, and therefore transition to turbulence in the acceleration stage will be triggered by the regular boundary-layer instability mechanism. Considering the very strong favourable pressure-gradient environment in the acceleration stage, the inception of turbulence in solitary wave boundary layers for earlier phases may differ quantitatively from that in oscillatory boundary layers.

In figure 13, the maximum value of the r.m.s. value of the fluctuating bed shear stress is plotted as a function of Re. As seen, turbulence grows explosively after Re reaches $Re \simeq 5 \times 10^5$. The time histories of the bed shear stress in combination with the flow visualization tests indicate that this transition is related to the inception of turbulent spots.

Vittori & Blondeaux (2008b, figure 6) plotted their DNS results regarding the transition to turbulence in terms of two non-dimensional parameters, namely H/h and δ_{VB}/h. Their data were recast (using the small-amplitude solitary wave theory;

https://doi.org/10.1017/S0022112009992837 Published online by Cambridge University Press

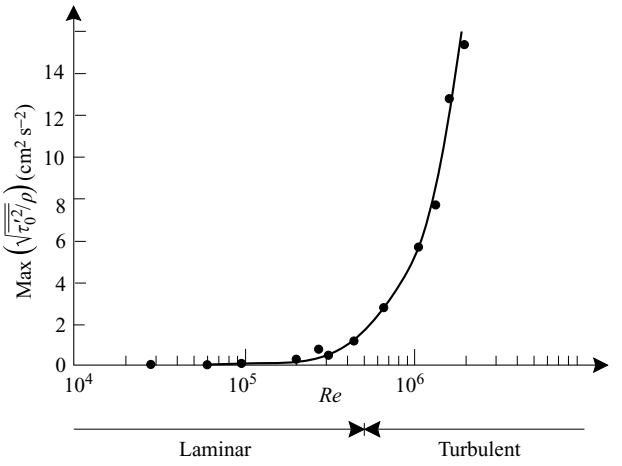


FIGURE 13. Maximum value of the r.m.s. value of the fluctuating bed shear stress as a function of Re. The time histories of the bed shear stress in combination with the flow visualization tests indicate that the laminar-to-turbulent transition at $Re \simeq 5 \times 10^5$ is related to the inception of turbulent spots.

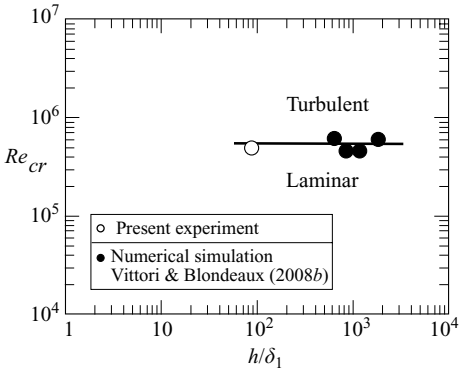


FIGURE 14. Transition to turbulence on the $(Re_{cr},\ h/\delta_1)$ plane. Re_{cr} is expected to increase with decreasing h/δ_1 for small values of h/δ_1.

(14) and (17)) and are plotted together with the present result on the plane $(Re,\ h/\delta_1)$ in figure 14 where h, the water depth, is taken as the half-height of the tunnel of the present experiment, and δ_1 is the Stokes length; (8). The present data and Vittori & Blondeaux's (2008*b*) numerical data seem to be in good agreement. It may be noted that Re_{cr} is expected to increase with decreasing values of h/δ_1 for small h/δ_1, similar to oscillatory boundary layers (e.g. Lodahl *et al.* 1998, figure 3, and Tuzi & Blondeaux 2008, figure 24).

It appears that there is a substantial delay in the laminar-to-turbulent transition in terms of the Reynolds number in the present case (c.f. $Re_{cr} \simeq 5 \times 10^5$ of the present case and $Re_{cr} = 1.5 \times 10^5$ of the oscillatory-boundary-layer case, see part 1). This is mainly because the adverse pressure gradient towards the end of the motion, a key factor in the transition, is more gentle in the present case than in the case of oscillatory motion.

https://doi.org/10.1017/S0022112009992837 Published online by Cambridge University Press

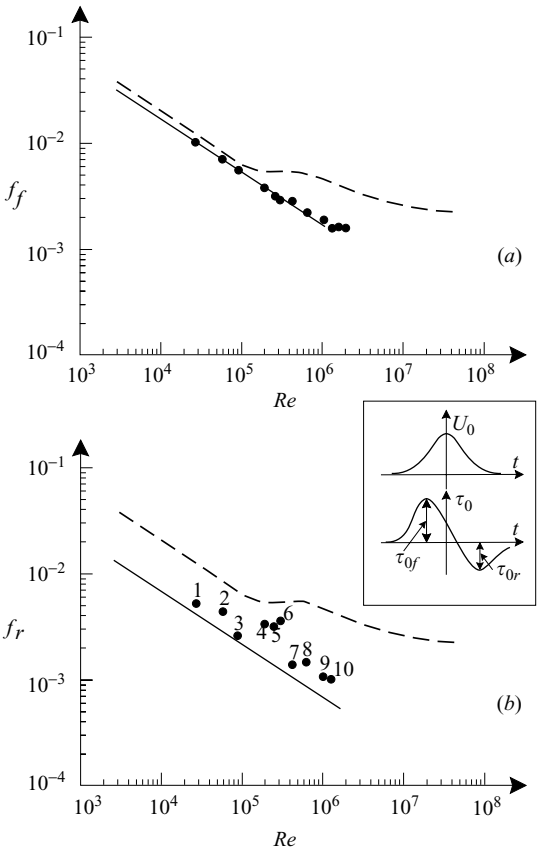


FIGURE 15. (*a*) Friction coefficient associated with the maximum bed shear stress in the acceleration stage where the near-bed flow is in the forward direction. (*b*) Friction coefficient associated with the maximum bed shear stress in the deceleration stage where the near-bed flow is in the reverse direction. Circles represent present experiments. Solid lines denote Liu *et al.*'s (2007) laminar solution. Dashed lines denote Jensen *et al.*'s (1989) experiments (oscillatory flow case) plotted as a reference line. Data points 1–3 lie in the laminar-regime Re range; 4–6 in the laminar-regime Re range with vortex tubes being present; and 7–10 in the transitional-regime Re range.

5. Flow resistance

The wave friction coefficient (first introduced by Lundgren & Jonsson 1961) is a key quantity in the analysis of oscillatory wave boundary layers. Drawing an analogy to oscillatory wave boundary layers, two friction coefficients can be defined for solitary-wave boundary layers: (i) Friction coefficient associated with the maximum bed shear stress in the acceleration stage where the near-bed flow is in the forward direction (figure 15*a*):

$$f_f = \frac{2\overline{\tau}_{0f}}{\rho U_{0m}^2} \tag{9}$$

and (ii) that associated with the maximum bed shear stress in the deceleration stage where the near-bed flow is in the reverse direction (figure 15*b*):

$$f_r = \frac{2\,|\overline{\tau}_{0r}|}{\rho U_{0m}^2}. \tag{10}$$

https://doi.org/10.1017/S0022112009992837 Published online by Cambridge University Press

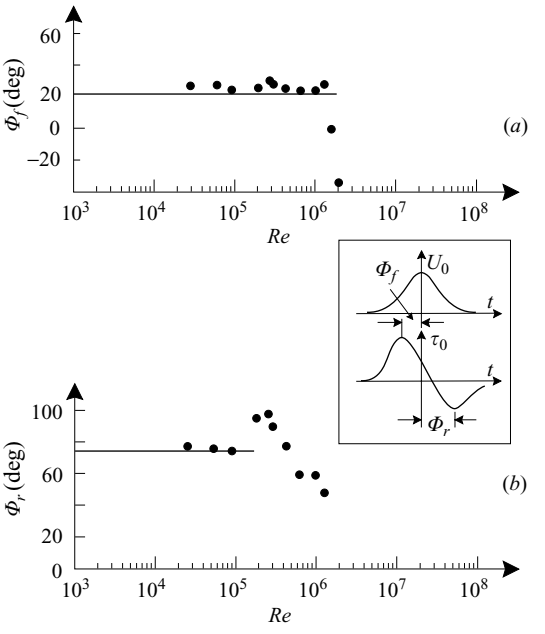


FIGURE 16. (*a*) Phase difference between the maximum value of the bed shear stress in the acceleration stage and that of the free-stream velocity. (*b*) Phase difference between the maximum value of the bed shear stress in the deceleration stage and that of the free-stream velocity. Circles represent present experiments. Solid lines denote Liu *et al.*'s (2007) laminar solution.

The flow-resistance data obtained from the present experiments related to both f_f and f_r are plotted in figure 15 together with Liu *et al.*'s (2007) laminar solution (the solid lines). Jensen *et al.*'s (1989) oscillatory-flow data also are plotted in the latter figures as a reference line (the dashed lines). These friction-coefficient diagrams are accompanied with the phase diagrams in figure 16, where Φ_f is the phase lead of the maximum bed shear stress in the acceleration stage over the maximum free-stream velocity, and Φ_r is the phase difference between the maximum free-stream velocity and the maximum bed shear stress associated with the reverse flow in the deceleration stage. The latter figure also includes Liu *et al.*'s (2007) laminar solutions for Φ_f and Φ_r (the solid lines).

From figure 15(*a*), it is seen that the agreement between the experiments and Liu *et al.*'s laminar solution is very good, even for values of the Reynolds number up to $Re = 1.3 \times 10^6$, a Reynolds number well beyond $Re_{cr} \simeq 5 \times 10^5$. This is because, even for such large Reynolds numbers ($Re = 6.5 \times 10^5$, 1.1×10^6 and 1.3×10^6), the flow remains in the laminar regime for the phase value where the shear stress attains its maximum value (c.f. figure 12*d*,*e*), and therefore the maximum bed shear stress (and therefore f_f) behaves like in the case of the laminar flow, revealing the observed agreement.

The present friction coefficient data in figure 15(*a*) are quite close to those of Jensen *et al.*'s (1989) oscillatory flow data, and this is for Re up to $Re = 1.5 \times 10^5$, the critical Reynolds number for the oscillatory-motion boundary layer, because the solitary-motion boundary-layer flow and the oscillatory-motion boundary-layer flow are quite similar for ωt up to the point where the near-bed flow reverses, and therefore

https://doi.org/10.1017/S0022112009992837 Published online by Cambridge University Press

the corresponding friction coefficients appear to be quite close to each other until the point of turbulent transition for the oscillatory-motion boundary layer is reached.

Regarding the friction coefficient for the reversed flow (figure 15*b*), the present data corresponding to the laminar regime (points 1–3) agree fairly well with laminar solution of Liu *et al.* (2007). For the three other data points in the laminar regime $Re < 5 \times 10^5$ (points 4–6), the friction coefficient is predicted to be relatively larger. This is because of the presence of the dips (B in figure 5*b*) in the bed shear stress traces, which is induced by the vortex tubes as described in the preceding paragraphs. For higher Re numbers ($Re > 5 \times 10^5$, the transitional regime), points 7–10 in figure 15(*b*), the experimental data differ from the laminar solution, as expected. Note that the data for the two highest Re numbers ($Re = 1.6 \times 10^6$ and 2×10^6) of the present experiments are not included in the diagram on grounds that the maximum value of $|\overline{\tau}_{0r}|$ could not be captured in the mean bed shear stress variations (see e.g. figure 12*f*, left).

Figure 16(*a*) shows that the present phase data, Φ_f, in the laminar regime are in fairly good agreement with the laminar solution of Liu *et al.* (2007) although there is a tendency that the experimental values are, in general, slightly larger than the prediction of the laminar theory. Regarding the two data points corresponding to the two highest Reynolds numbers in figure 16(*a*), the phase becomes almost zero for $Re = 1.6 \times 10^6$, and even negative for $Re = 2 \times 10^6$. This is because of the turbulence, as seen clearly from e.g. figure 12(*f*, left). Although not captured in the present experiments due to the experimental constraint (the finite stroke length of the piston), Φ_f is expected to 'recover' again with a further increase in Re as the turbulence spreads further towards the smaller values of ωt in the fully developed turbulent regime, and it is expected to settle at a positive value, albeit smaller than $\omega t = 20^\circ$ (the laminar-regime phase lead), similar to the behaviour of the phase lead observed in the case of the oscillatory flow (see e.g. Jensen *et al.* 1989; figure 11*b*).

As for Φ_r (figure 16*b*), the agreement between the experiment and Liu *et al.*'s laminar solution is very good in the laminar-regime Reynolds number range for the first three data points. However, Φ_r data for the next three points in the laminar regime deviate from Liu *et al.*'s laminar solution because these data points correspond to the laminar regime with vortex tubes ($Re = 2 \times 10^5$, $Re = 2.7 \times 10^5$ and $Re = 3.1 \times 10^5$). For the transitional Reynolds number range ($Re > 5 \times 10^5$), figure 16(*b*) shows that Φ_r decreases with respect to the values experienced in the laminar regime. This is because of the introduction of turbulence via the appearance of turbulent spots at the phase values where the maximum bed shear stress in the deceleration stage is experienced. However, as the Reynolds number is increased further, Φ_r is expected to pick up values larger than those experienced in the laminar and transitional regimes exhibited in figure 16(*b*) simply because the flow reversal in this case will be delayed due to turbulence, resulting in values of Φ_r larger than the laminar and transitional ones. Similar to figure 15(*b*), the Φ_r data for the two highest Re numbers ($Re = 1.6 \times 10^6$ and 2×10^6) of the experiment are not included in figure 16(*b*) on grounds that the maximum value of $|\overline{\tau}_{0r}|$ could not be captured in the experiments.

Finally, figure 17 displays the phase data regarding the phase at which the flow reversal takes place at the bed, Φ_c. Again the experiment and the laminar solution are in very good agreement. The boundary layer reverses in the laminar regime until Re reaches the value $Re = 1.3 \times 10^6$ because only after this Reynolds number the turbulence on average will reach the phase where the flow reversal takes place (figures 12*e*) although transition to turbulence occurs much earlier, i.e. at a much lower Reynolds number, $Re = 5 \times 10^5$. Once turbulence reaches that point, the reversal

https://doi.org/10.1017/S0022112009992837 Published online by Cambridge University Press

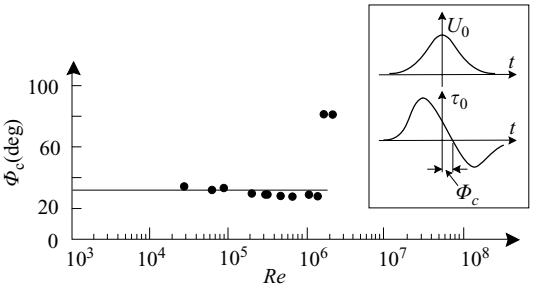


FIGURE 17. Phase data regarding the phase at which the flow reversal takes place. Solid line denotes Liu *et al.*'s (2007) laminar solution.

will occur in the turbulent regime, and this will delay the flow reversal, revealing the higher values of Φ_c around 80°, observed for the two highest Reynolds numbers in the tests (figure 17). The flow reversal at the bed delays quite considerably in the case of the turbulent regime, similar to oscillatory-flow boundary-layer flows (part 1); this is related to the continuous supply of momentum-rich fluid from the outer flow as discussed in part 1.

6. Velocity profiles

Figure 18 displays the phase evolution of the mean velocity profiles at three different Reynolds numbers, $Re = 7.1 \times 10^4$, $Re = 4.8 \times 10^5$ and $Re = 1.8 \times 10^6$, the first being in the laminar regime, the second at the onset of turbulent transition and the third in the transitional regime. Figure 18 also includes Liu *et al.*'s (2007) laminar solution for the phase values $\omega t = -100°$, $-40°$, $100°$ and $40°$ (figure 18*a*). We note that the agreement between the present laminar velocity profiles and Liu *et al.*'s (2007) laminar solution is fairly good. From figure 18, it is clearly seen that the flow reversal occurs at larger and larger ωt values with the distance from the bed, similar to oscillatory boundary layers (e.g. Jensen *et al.* 1989). It is also seen that the flow reversal across the depth is, as expected, delayed quite substantially when Re is increased from $Re = 4.8 \times 10^5$ to 1.8×10^6, in agreement with the bed shear stress measurements (see figure 17; see also the discussion in conjunction with the delay in the flow reversal due to turbulence in the preceding paragraphs and in part 1).

Figure 19 presents the phase evolution of the mean velocity profiles in semi-logarithmic plot for $Re = 1.8 \times 10^6$. The velocity and the vertical distance from the bed are normalized in terms of the inner-flow parameters, $U_f (= \sqrt{\overline{\tau}_0/\rho})$, the phase-resolved mean friction velocity, and ν, the kinematic viscosity:

$$y^+ = \frac{yU_f(\omega t)}{\nu} \quad \text{and} \quad \overline{u}^+(y, \omega t) = \frac{\overline{u}(y, \omega t)}{U_f(\omega t)}. \tag{11}$$

In figure 19, we also plot the van Driest velocity profile (van Driest 1956)

$$\overline{u}^+ = 2\int_0^{y^+} \frac{\mathrm{d}y^+}{1 + \left\{1 + 4\varkappa^2 y^{+2}\left[1 - \exp\left(-\frac{y^+}{A_d}\right)\right]^2\right\}^{1/2}} \tag{12}$$

as a reference line. Here $\varkappa$ is the von Kármán constant ($= 0.4$), and A_d is the van Driest damping factor ($= 25$). Note that the van Driest profile ($\overline{u}^+$ in (12)) tends to

https://doi.org/10.1017/S0022112009992837 Published online by Cambridge University Press

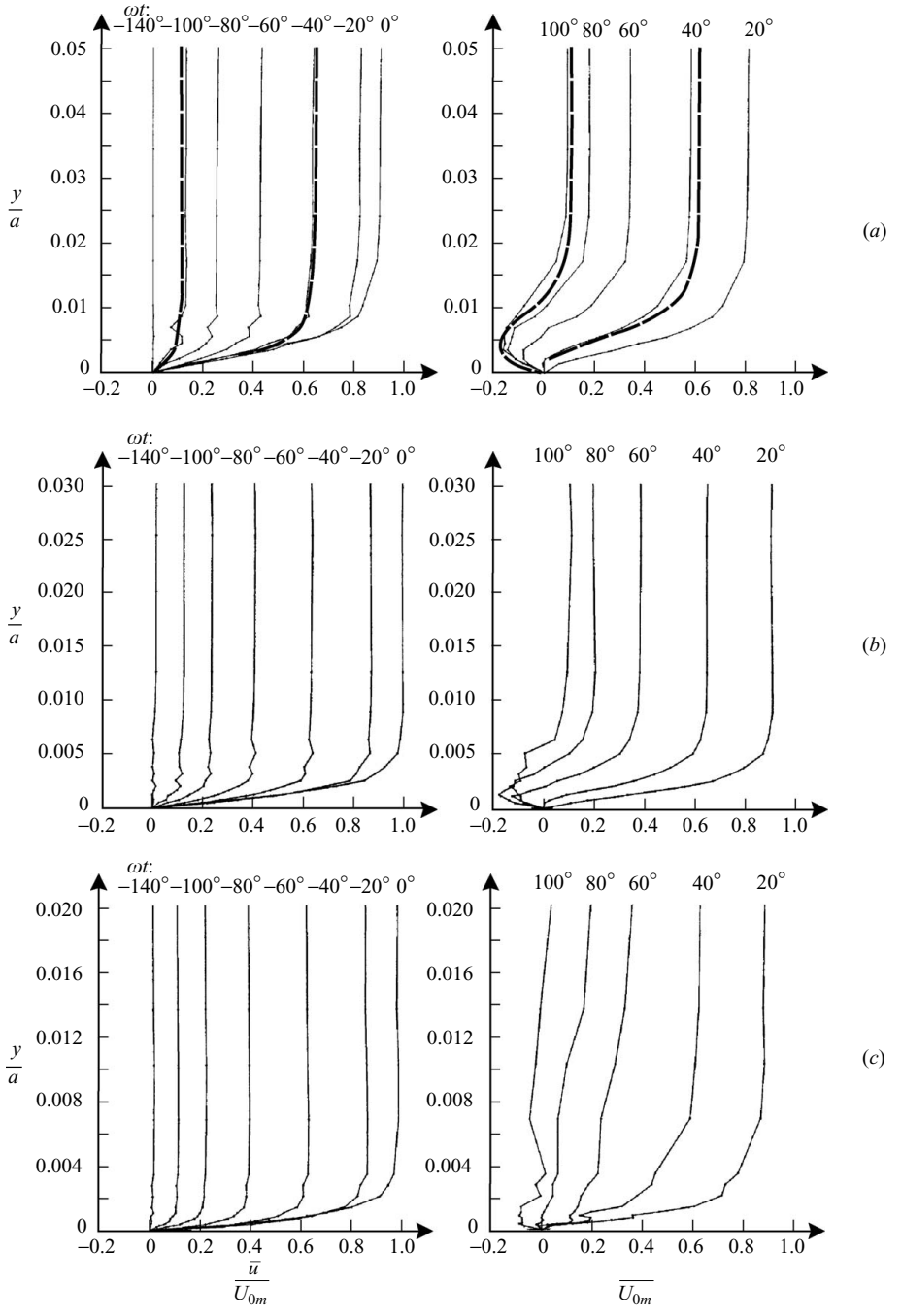


FIGURE 18. Phase evolution of the mean velocity profiles at three different Reynolds numbers: (*a*) $Re = 7.1 \times 10^4$, (*b*) $Re = 4.8 \times 10^5$ and (*c*) $Re = 1.8 \times 10^6$, the first being in the laminar regime, the second at the onset of turbulent transition and the third in the transitional regime. Solid lines represent present experiments and dashed lines in (*a*) denote Liu *et al.*'s (2007) laminar solution.

https://doi.org/10.1017/S0022112009992837 Published online by Cambridge University Press

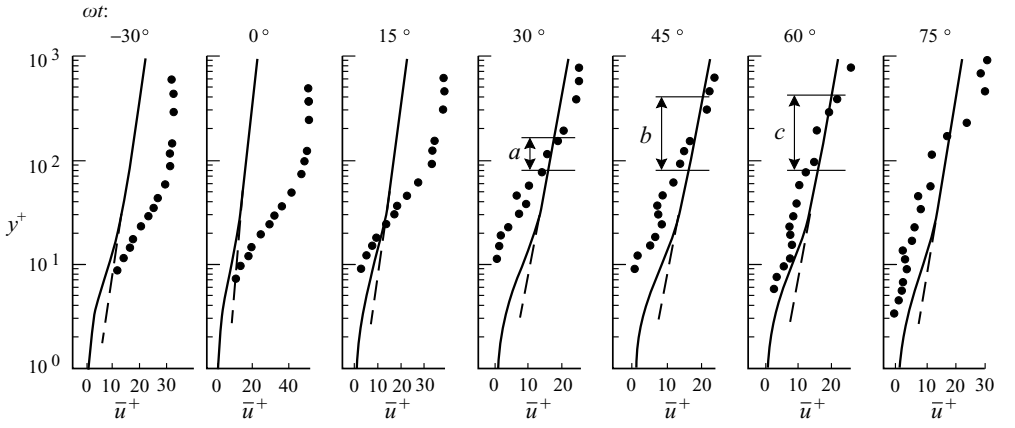


FIGURE 19. Phase evolution of the mean velocity profiles in semi-logarithmic plot. $Re = 1.8 \times 10^6$. The velocity and the vertical distance from the bed are normalized in terms of the inner-flow parameters. Circles represent present data. Solid lines denote van Driest velocity profile; (12). Dashed line denotes logarithmic velocity distribution $\overline{u}^+ = (1/\varkappa)\ln y^+ + 5$.

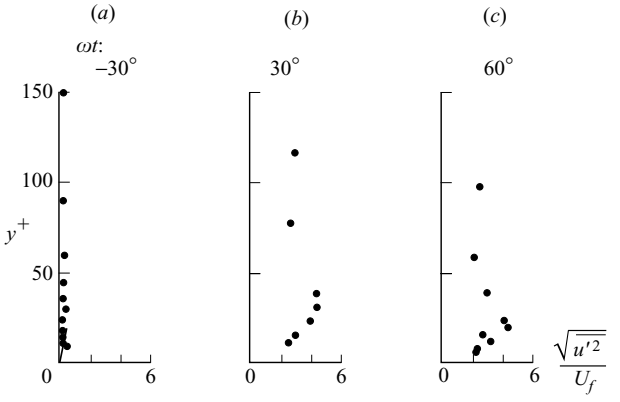


FIGURE 20. (*a–c*) The time development of the turbulence in terms of the r.m.s. value of the fluctuating component of u, normalized by the phase-resolved friction velocity, as a function of the distance y^+. $Re = 1.8 \times 10^6$.

the logarithmic distribution $\overline{u}^+ = (1/\varkappa)\ln y^+ + 5$ for large values of y^+ (the dashed lines in figure 19).

The y^+ interval over which the measured velocity profile comes closest to the logarithmic distribution is marked *a*, *b* and *c* (over the phase interval $\omega t \simeq 30°$–$60°$) in figure 19. Although the behaviour of the measured velocity distribution as a function of phase is qualitatively quite similar to that of oscillatory boundary-layer flows (discussed in greater details by Sumer, Jensen & Fredsøe 1987, and Jensen *et al.* 1989, p. 279 and figure 17), the agreement between the velocity data and the logarithmic distribution over the phase interval $\omega t \simeq 30°$–$60°$ is not very good. This may be attributed to the fact that the boundary layer in the experiment (test 14, $Re = 1.8 \times 10^6$) is not in the fully developed turbulent regime.

Figure 20(*a–c*) illustrates the time development of the turbulence in terms of the r.m.s. value of the fluctuating component of u, normalized by the phase-resolved mean bed shear stress velocity, as a function of the distance y^+. This is for the

https://doi.org/10.1017/S0022112009992837 Published online by Cambridge University Press

experiment where $Re = 1.8 \times 10^6$. Clearly, no turbulence has yet been generated at $\omega t = -30^\circ$ (or before). However, by the time the phase reaches the value $\omega t = 30^\circ$, a substantial amount of turbulence has been produced, and this turbulence has spread across the depth (up to large values of y^+). As this Reynolds number ($Re = 1.8 \times 10^6$) is still in the transitional regime, the turbulence profiles given in this figure cannot represent those in the fully developed turbulent regime simply because both the r.m.s. value of u' and the bed shear stress velocity U_f have not yet attained their fully developed regime values. Therefore, no direct comparison can be made between the measured distributions in figure 20 and the corresponding steady boundary-layer (e.g. Monin & Yaglom 1973) and the oscillatory boundary-layer distributions (e.g. Jensen *et al.* 1989). Nevertheless, it may be noted that the measured distribution of $\sqrt{\overline{u'^2}}/U_f$ attains a maximum value at $y^+ = 20$–25 (figure 20*b*,*c*), in agreement with the steady and oscillatory boundary-layer results. However, the present values of $\sqrt{\overline{u'^2}}/U_f$ are generally a factor of 2 larger than those of the steady and oscillatory boundary layers.

7. Remarks on practical applications

For a small-amplitude solitary water wave, the surface elevation and the horizontal particle velocity are, respectively, given as

$$\eta = H\,\mathrm{sech}^2(\omega t), \tag{13}$$

$$U_0 = U_{0m}\,\mathrm{sech}^2(\omega t), \tag{14}$$

in which U_{0m} and ω are

$$U_{0m} = \sqrt{gh}\,\frac{H}{h}, \tag{15}$$

$$\omega = \sqrt{\frac{3}{4}gH}\,\frac{1}{h}, \tag{16}$$

in which H is the wave height and h is the water depth. Similar to (2), a period can be defined by

$$T = \frac{2\pi}{\omega} = 2\pi\sqrt{\frac{4}{3gH}}\,h, \tag{17}$$

where T can be interpreted as a time scale that characterizes the width of the free-stream velocity time series as in figure 1(*a*).

The boundary layer developing over a smooth bed under a solitary wave where the half-space approximation is valid ($y > 0$; see § 4.1) is described by a single non-dimensional quantity, namely the Reynolds number, defined by (7) in which U_{0m} is given by (15) and a by (6), (16) and (17).

In the case when T is large, so large that the boundary-layer thickness becomes comparable to the water depth, the parameter water-depth-to-boundary-layer-thickness ratio should also be involved, as pointed out above. This case normally involves turbulent-regime boundary-layer flows (not only in the field but also, to a large extent, in the laboratory). The boundary-layer thickness, δ_t, in this case may be estimated as follows. Note that δ_t corresponding to T may be written as

$$\delta_t = O(\sqrt{2\nu_t T}), \tag{18}$$

https://doi.org/10.1017/S0022112009992837 Published online by Cambridge University Press

in which ν_t is the turbulent diffusion coefficient and may, to a first approximation, be taken as

$$\nu_t = O\left(\frac{\varkappa}{6}\delta_t U_{fm}\right), \tag{19}$$

in which $\varkappa$ is the von Kármán constant ($\simeq 0.4$), and U_{fm} is the maximum value of the friction velocity.

(Equation (19) is obtained by integrating the turbulent diffusion coefficient over the boundary-layer thickness, $\nu_t = \frac{1}{\delta_t}\int_0^{\delta_t} \varepsilon(y)\,\mathrm{d}y$, with $\varepsilon(y)$ obtained from the Reynolds analogy (i.e. the transfer of momentum and mass is analogous, e.g. Sayre 1968, p. 11) as $\varepsilon(y) = \kappa U_{fm} y(1-(y/\delta_t))$.)

Now, solving the boundary-layer thickness from (18) and (19), δ_t is

$$\delta_t = O(0.1 U_{fm} T). \tag{20}$$

In the present experiments, the largest boundary-layer thickness was, from the preceding equation, $\delta_t = O(0.1 U_{fm} T) = O(0.1 \times 2.8\,\mathrm{cm\,s^{-1}} \times 8.5\,\mathrm{s}) = O(2.4\,\mathrm{cm})$ in test 15 corresponding to the highest Reynolds number, and hence $h/\delta_t = O(14.5\,\mathrm{cm}/2.4\,\mathrm{cm}) = O(6)$ where h is taken as $h = 29/2 = 14.5$ cm, the half-height of the tunnel (figure 1 in part 1). It may be noted that the above estimate of the boundary-layer thickness agrees quite well with that found from the measured velocity profiles (figure 18).

So, the ratio h/δ_t in test 15 was like $O(6)$, large enough for the parameter h/δ_t not to be very significant. (h/δ_t was even larger in the other tests.) Therefore, the results of the present study are directly applicable to boundary layers developing under a solitary wave provided that the wave period is not very large so that the water-depth-to-boundary-layer-thickness ratio remains sufficiently large. Otherwise, the boundary-layer properties should be dependent not only on Re but also on the water-depth-to-boundary-layer-thickness ratio.

The present tests cover the smooth-bed case. In the case of a rough bed, there will be a third parameter, a/k_s, in which k_s is Nikuradse's equivalent sand roughness. For the present results to be applicable for the rough-bed case, the bed should act as a hydraulically smooth boundary, i.e. $k_s U_{fm}/\nu$ should be sufficiently small, certainly smaller than $O(10)$. Note that so far no data are available for solitary motion/wave boundary layers over rough beds.

8. Conclusions

(*a*) The experiments show that the critical value of the Reynolds number for transition to turbulence is $Re_{cr} = 5 \times 10^5$.

(*b*) In a narrow sub-range of Re number ($2 \times 10^5 < Re < 5 \times 10^5$) in the laminar regime, a regular array of vortices appear near the bed as a result of the inflectional-point shear layer instability.

(*c*) The transition to turbulence at $Re_{cr} = 5 \times 10^5$ is associated with the appearance of turbulent spots, similar to oscillatory-motion boundary-layer flows. The passage of turbulent spots is marked in the bed shear stress by single, or multiple, or sometimes quite dense spikes. With these spikes, the instantaneous value of the bed shear stress is increased tremendously. Clearly, this has important implications for sediment transport.

(*d*) Flow resistance in terms of wave friction coefficient including the phase information has been worked out for both the acceleration and deceleration stages of the solitary motion (figures 15 and 16).

https://doi.org/10.1017/S0022112009992837 Published online by Cambridge University Press

(*e*) The near-bed flow reverses during the deceleration stage of the free stream, a result similar to that in oscillatory-motion boundary-layer flows. The flow reversal occurs at smaller and smaller ωt values as one moves towards the bed.

(*f*) The flow reversal is delayed quite substantially with increasing Re.

This study has been partially funded by (i) the Danish Research Council for Technology and Production Sciences (FTP) under the research program Exploitation and Protection of Coastal Zones (EPCOAST), and (ii) the Danish Council for Strategic Research through the research programme 'Seabed and Wind Farm Interaction'. P.L.F.L. acknowledges the support from NSF and ONR through grants to Cornell University. Comments of Professor Giovanna Vittori and other two anonymous referees are also appreciated.

Supplementary movies available at journals.cambridge.org/flm.

REFERENCES

Carstensen, S., Sumer, B. M. & Fredsøe, J. 2010 Coherent structures in wave boundary layers. Part 1. Oscillatory motion. *J. Fluid Mech.* **646**, 169–206.

Costamagna, P., Vittori, G. & Blondeaux, P. 2003 Coherent structures in oscillatory boundary layers. *J. Fluid Mech.* **474**, 1–33.

Fredsøe, J. & Deigaard, R. 1992 *Mechanics of Coastal Sediment Transport*. World Scientific.

Fredsøe, J., Sumer, B. M., Kozakiewicz, A., Chua, L. H. C. & Deigaard, R. 2003 Effect of externally generated turbulence on wave boundary layer. *Coastal Engng* **49**, 155–183.

Jensen, B. L., Sumer, B. M. & Fredsøe, J. 1989 Turbulent oscillatory boundary layers at high Reynolds numbers. *J. Fluid Mech.* **206**, 265–297.

Keulegan, G. H. 1948 Gradual damping of solitary wave. *J. Res. Natl. Bur. Stand.* **40**, 607–614.

Liu, P. L.-F. 2006 Turbulent boundary-layer effects on transient wave propagation in shallow water. *Proc. Roy. Soc.* A **462**, 3431–3491.

Liu, P. L.-F. & Orfila, A. 2004 Viscous effects on transient long-wave propagation. *J. Fluid Mech.* **520**, 83–92.

Liu, P .L.-F., Park, Y. S. & Cowen, E. A. 2007 Boundary layer flow and bed shear stress under a solitary wave. *J. Fluid Mech.* **574**, 449–463.

Lodahl, C., Sumer, B. M. & Fredsøe, J. 1998 Turbulent combined oscillatory flow and current in a pipe. *J. Fluid Mech.* **373**, 313–348.

Lundgren, H. & Jonsson, I. G. 1961 Bed shear stress induced by a wave motion. Coastal Engineering Laboratory, Technical University of Denmark, Basic Research – Progress Report 1, pp. 3–5.

Mei, C. C. 1983 *The Applied Dynamics of Ocean Surface Waves*. John Wiley & Sons.

Monin, A. S. & Yaglom, A. M. 1973 *Statistical Fluid Mechanics: Mechanics of Turbulence*, vol. 1. MIT Press.

Sayre, W. W. 1968 Dispersion of mass in open-channel flow. Hydraulics papers, no. 3, Colorado State University, Fort Collins. (The material contained in this publication is identical to the dissertation of the same title submitted in March 1967 to Colorado State University in partial fulfilment of the requirements for the degree of Doctor of Philosophy in Civil Engineering.)

Sumer, B. M., Jensen, B. L. & Fredsøe, J. 1987 Turbulence in oscillatory boundary layers. *In Advances in Turbulence* (ed. Gt. Comte-Bello & J. Mathieu), pp. 556–567. Springer.

Sumer, B. M., Jensen, P. M., Sørensen, L. B., Fredsøe, J. & Liu, P. L.-F. 2008 Turbulent solitary wave boundary layer. In *Proceedings of the 18th International Offshore (Ocean) and Polar Engineering Conference (ISOPE)*, pp. 775–781. Vancouver, British Columbia, Canada.

Tanaka, H., Sumer, B. M. & Lodahl, C. 1998 Theoretical and experimental investigation on laminar boundary layers under cnoidal wave motion. *Coastal Engng J.* **40** (1), 81–98.

https://doi.org/10.1017/S0022112009992837 Published online by Cambridge University Press

TUZI, R. & BLONDEAUX, P. 2008 Intermittent turbulence in a pulsating pipe flow. *J. Fluid Mech.* **599**, 51–79.

VAN DRIEST, E. R. 1956 On turbulent flow near a wall. *J. Aeronaut. Sci.* **23**, 1007–1011.

VITTORI, G. & BLONDEAUX, P. 2008*a* Boundary layer flow and bed shear stress under solitary wave. In *Book of Abstract of the 31st International Conference on Coastal Engineering*. Hamburg, Germany, Abstract No. 062.

VITTORI, G. & BLONDEAUX, P. 2008*b* Turbulent boundary layer under a solitary wave. *J. Fluid Mech.* **615**, 433–443.

https://doi.org/10.1017/S0022112009992837 Published online by Cambridge University Press